AIAA JOURNAL
Vol. 52, No. 6, June 2014

Corotational Formulation for Bonded Joint Finite Elements

Scott E. Stapleton* and Anthony M. Waas†
University of Michigan, Ann Arbor, Michigan 48109
and
Steven M. Arnold‡ and Brett A. Bednarcyk§
NASA John H. Glenn Research Center at Lewis Field, Cleveland, Ohio 44135

DOI: 10.2514/1.J052422

Enhanced finite elements are elements with an embedded analytical solution that can capture detailed local fields, enabling more efficient mesh independent finite element analysis. In earlier research, this method was applied to adhesively bonded joints. The adherends were modeled as composite Euler–Bernoulli beams, and the adhesive layer was modeled as a bed of linear shear and normal springs. The field equations were derived using the principle of minimum potential energy, and the resulting solutions for the displacement fields were used to generate shape functions and a stiffness matrix for a single bonded joint finite element. In this study, the capability to model large rotations and nonlinear adhesive constitutive behavior is developed, and progressive failure of the adhesive is modeled by remeshing the joint as the adhesive fails. The results obtained using this enhanced joint element are compared with experimental results.

Nomenclature

$\mathbf{B}$	=	matrix relating adherend strains to nodal deformations
$b_{i,ai}$	=	width of ith adherend (subscript i) or adhesive (subscript ai)
C_1	=	crack scaling constant
C_2	=	constant relating adhesive axial stress to strain
$C_{3,4}$	=	constants relating adhesive shear and peel strain to bulk adhesive tensile strain data
c, s	=	$\cos\phi$, $\sin\phi$
$\mathbf{D}$	=	material tangent stiffness matrix of the element
E_{ai}	=	Young's modulus of ith adhesive
$\hat{\boldsymbol{f}}^{\text{Int,Ext}}$	=	internal and external load vector of the element
$\mathbf{G}$	=	matrix relating adherend strains to deformations, where subscripts i and ai may be used to refer to the ith adherend or adhesive, respectively
$G_{1,2}$	=	mode 1 and 2 fracture energy release rates, with the subscript C denoting a critical value
$\mathbf{I}$	=	3×3 identity matrix
$\hat{\mathbf{k}}$	=	local stiffness matrix of the element
$\mathbf{k}_{\text{mat,geo}}$	=	global material and geometric stiffness matrix of the element
l	=	original length of element
$l_{\text{crack}}^{\text{prev}}$	=	length of a crack within an adhesive layer of an element at the previous load step
$l_{\text{crack}}^{\text{cur}}$	=	length of a crack within an adhesive layer of an element at the current load step
l_1	=	deformed length of first adherend, and additional subscript refers to x or z component
$\mathbf{N}$	=	elemental shape functions
N	=	number of adherends in the joint element
$\boldsymbol{q}$	=	nodal displacements
$\boldsymbol{q}_{\text{def}}$	=	local nodal deformations of an element
$\boldsymbol{q}^i$	=	nodal displacements of adherend i
q_k^{ij}	=	nodal displacement component k (where $k = 1, 2$, or 3 is horizontal, vertical, or rotational displacement) of adherend i and side j (where $j = l$ or r, meaning the left or right side of the adherend)
$\boldsymbol{q}_r$	=	rigid body nodal displacements resulting from rigid body rotation of an element
$\boldsymbol{q}_{\text{rig}}$	=	rigid body nodal displacements of an element
$\boldsymbol{q}_t$	=	rigid body nodal displacements resulting from rigid body translation of an element
$\mathbf{T}_1$	=	orthogonal transformation matrix of a point
$\mathbf{T}_{1,\phi}$	=	modified transformation matrix of a point
t_i	=	thickness of ith adherend
$\hat{\boldsymbol{u}}$	=	vector of adherend centerline displacements, where subscripts i and ai may be used to refer to the ith adherend or adhesive, respectively
$u_i(\hat{x})$	=	local axial ($\hat{x}$ direction) deformation of adherend i
V	=	volume of the element
$W^{\text{Int,Ext}}$	=	internal and external work of the element
$w_i(\hat{x})$	=	local transverse ($\hat{z}$ direction) deformation of adherend i
$\boldsymbol{X}$	=	nodal position vector in the fixed global coordinate system of the undeformed state
$\boldsymbol{x}$	=	nodal position vector in the fixed global coordinate system of the deformed state
$\hat{\boldsymbol{x}}$	=	nodal position vector in the elemental local rotated coordinate system of the deformed state
$\hat{x}$	=	derivative with respect to $\hat{x}$
$\boldsymbol{x}^{ir}$	=	position vector of the right node of the ith adherend in the global coordinate system of the deformed state
η_{ai}	=	thickness of ith adhesive
ν_{ai}	=	Poisson's ratio of ith adhesive
$\hat{\boldsymbol{\sigma}}, \hat{\boldsymbol{\varepsilon}}$	=	stress and strain vectors of the element, where subscripts i and ai may be used to refer to the ith adherend or adhesive, respectively
$\hat{\sigma}_{ai}, \hat{\varepsilon}_{ai}$	=	local peel ($\hat{z}$ direction) stress and strain of adhesive i
$\hat{\sigma}_i, \hat{\varepsilon}_i$	=	local axial ($\hat{x}$ direction) stress and strain of adherend i

Presented as Paper 2012-1449 at the 53rd AIAA/ASME/ASCE/AHS/ASC SDM Conference, Honolulu, HI, 23–26 April 2012; received 21 November 2012; revision received 25 October 2013; accepted for publication 6 December 2013; published online 21 April 2014.

*Graduate Student, Department of Aerospace Engineering; currently Research Group Leader, Institute for Textile Technology, RWTH Aachen University, Aachen, Germany; sstaple@umich.edu. Student Member AIAA (Corresponding Author).

†Felix Pawlowski Collegiate Professor, Department of Aerospace Engineering; dcw@umich.edu. Fellow AIAA.

‡Chief, Mechanics and Life Prediction, 21000 Brookpark Rd.; Steven.M.Arnold@NASA.gov. Member AIAA.

§Material Research Engineer, 21000 Brookpark Rd.; Brett.A.Bednarcyk@NASA.gov. Associate Fellow AIAA.

$\sigma_{vm,Bulk}$ = von Mises equivalent stress and adhesive stress obtained from bulk adhesive tensile testing
$\hat{\tau}_{ai}, \hat{\gamma}_{ai}$ = local shear stress and strain of adhesive i
ϕ = angle of rigid body rotation of an element
$\phi_{1,\boldsymbol{q}}$ = vector resulting from approximating the variation of $\mathbf{T}$
ψ_i = shear to peel ratio of ith adhesive

I. Introduction

With the increased use of fiber reinforced composite materials, adhesively bonded joints become an increasingly important topic. As bonded joints increase in popularity and use, the demand for modeling techniques increases as well. In the past, analytical models have been favored as the preferred method of predicting stresses and strength [1–6], but finite element (FE) methods have emerged as the new standard in preliminary design due to the necessity of analyzing and designing components that contain multiple or complex joints where analytical techniques become intractable. FE based methods have been proven to be extremely powerful, but the small scale of the adhesive thickness when compared with the dimensions of the surrounding structure has kept joint FE analysis largely out of global vehicle models. A fine mesh is needed to correctly model the adhesive layer producing an incompatibility in simultaneously analyzing the joint stresses accurately in conjunction with a very coarse model of an entire vehicle. Therefore, the actual design and sizing of joints is often put off until a later time, when small submodels are used to investigate the details of a vehicle.

To address this problem, a bonded joint FE has been created [7–10] wherein an entire bonded joint can be modeled with a single element. This joint element considers the adherends to behave like beams (or wide panels) and the adhesive to be made up of a bed of shear and normal nonlinear springs. The governing equations of this structural model are found and solved to produce enhanced shape functions for the joint element. Furthermore, the element has been generalized to allow multiple adherend/adhesive layers and ply drops/thickness tapers, providing the capability to model a variety of joint types with very few elements.

This paper presents an extension of the joint element to model progressive failure of a joint and ultimately predict the strength using very few elements. Modern polymeric adhesives are usually highly nonlinear, causing linear elastic analysis to be insufficient. Furthermore, the eccentricity of many joint configurations results in large rotations under moderate loading [5,11,12], necessitating the consideration of nonlinear geometric effects.

Therefore, geometric nonlinear effects due to large rotations and material nonlinearity are both pivotal in predicting the strength of a joint. This paper extends the previously created joint element to include these additional effects. Additionally, a method of growing an adhesive crack internally within an element during the analysis will be presented in order to preserve the original intent of the joint element, which is to model a joint with very few elements.

Currently, the state of the art for modeling the progressive failure of joints involves using a dense mesh FE model (FEM) with damage mechanics methods like cohesive zone models (CZMs) or continuum damage mechanics [13]. Because the present joint element is merely a tool, it will accommodate using inputs derived from either of these philosophies to govern the stress-strain relation of the adhesive. A method to characterize the adhesive layer using either bulk adhesive tensile data (as someone would do when using the continuum damage mechanics approach), or fracture mechanics inputs like mode 1 strength and fracture toughness, will also be presented. The application of each will be demonstrated, and results will be compared with published experimental data.

II. Formulation

The formulation of the joint element has been divided into discrete parts, namely, the corotational formulation, material nonlinearity effects, crack growth, and adhesive constitutive modeling. Each section presents a formulation to address a certain requirement to realize progressive failure simulation of the joints. The corotational formulation addresses large rotations in joint problems, whereas material nonlinearities show how nonlinear constituents are modeled. The crack growth formulation deals with the failure of the adhesive layer. Finally, the last section illustrates a few methods of defining the properties of the adhesive based on several different experimental protocols.

A. A Corotational Formulation

Consider a structure consisting of N layers of thin plates under cylindrical bending joined together by $N-1$ thin layers of a much more compliant adhesive material (see Fig. 1a). The plates are assumed to behave as "wide" Euler Bernoulli beams (hence the cylindrical bending assumption, which corresponds to "plane strain" in classical elasticity). The adhesive joining the plates is modeled as a bed of uncoupled shear and peel nonlinear springs, which means that the displacements vary linearly in thickness direction and the shear and peel stresses are constant through the thickness. The plates can be isotropic, transversely isotropic, or a layered composite. The plates and adhesive are assumed to be under proportional loading and are modelled as nonlinear elastic materials.

A corotational formulation is used to capture large rotations and has been primarily adapted from previous work by Belytscheko and Hsieh [14] and Crisfield and Moita [15]. This formulation tracks the rigid body rotation of an element through a local rotational coordinate system and considers the rotations and deformations measured with respect to this rotated frame of reference to be small. The main benefit of this formulation is that the previously implemented code for the small rotation problem [8–10] can be used in subsequent calculations.

The element has $2N$ nodes located at the boundaries of the centerline of the plates (numbered as shown in Fig. 1b), and the nodal displacements are defined as

$$\boldsymbol{q} = [\,\boldsymbol{q}^1 \quad \ldots \quad \boldsymbol{q}^i \quad \ldots \quad \boldsymbol{q}^N\,]^T \tag{1}$$

where the superscript represents the adherend or plate, and

$$\boldsymbol{q}^i = [\,q_1^{il} \quad q_2^{il} \quad q_3^{il} \quad q_1^{ir} \quad q_2^{ir} \quad q_3^{ir}\,] \tag{2}$$

refers to the horizontal, vertical, and rotational displacements of the left and right nodes in plate i, respectively.

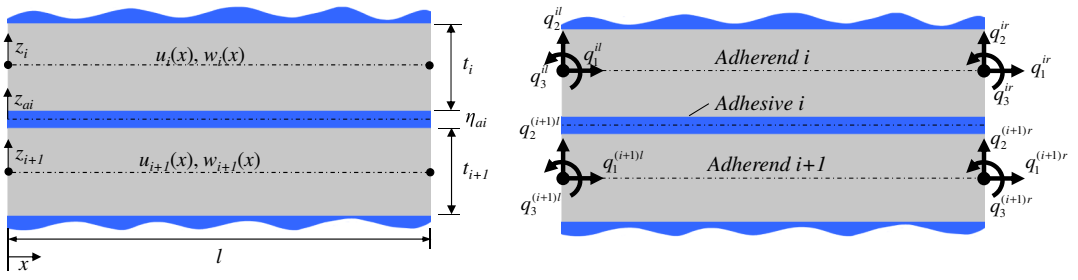

a) b)

Fig. 1 Overlap region of an adhesively bonded joint with multiple bonded layers: a) geometric parameters (width in the y direction is b) and b) FE discretization.

1. Rigid Body Displacements

The element has a local rotated coordinate system, $\hat{\boldsymbol{x}}$, which is rotated and translated relative to the fixed coordinate system, $\boldsymbol{x}$, by angle ϕ and vector $\boldsymbol{q}_t^{1l}$, respectively (Fig. 2). The translation and rotation will be properly defined later. The nodal displacements of the element in the fixed coordinate system can be decomposed into rigid body displacements, $\boldsymbol{q}_{\text{rig}}$, and displacements which only cause deformation in the body, $\boldsymbol{q}_{\text{def}}$, with the relation

$$\boldsymbol{q} = \boldsymbol{q}_{\text{rig}} + \boldsymbol{q}_{\text{def}} \tag{3}$$

The rigid body nodal displacements, $\boldsymbol{q}_{\text{rig}}$, can be further decomposed into rigid body displacements resulting from rigid body rotation, $\boldsymbol{q}_r$, and displacements resulting from rigid body translation, $\boldsymbol{q}_t$:

$$\boldsymbol{q}_{\text{rig}} = \boldsymbol{q}_t + \boldsymbol{q}_r \tag{4}$$

The translational rigid body displacements, $\boldsymbol{q}_t$, are defined as

$$\boldsymbol{q}_t = [\,\boldsymbol{q}_t^{1l} \quad \ldots \quad \boldsymbol{q}_t^{1l}\,]^T \tag{5}$$

which is simply made up of a rigid body displacement and rotation for each node, where the rigid body displacement and rotation of each node is defined as the horizontal and vertical displacements of the left node of the first adherend (reference node, see Fig. 2a) and the rotation of the left node of the first adherend:

$$\boldsymbol{q}_t^1 = [\,q_1^{1l} \quad q_2^{1l} \quad \phi\,] \tag{6}$$

Although the rotation is not necessarily part of the rigid body translation, it is more convenient to insert it into the translational rigid body displacements because each adherend will be rigidly rotated by the angle ϕ.

To find the rigid body displacements due to the rotation of the element about the first node, consider the right node of the ith adherend, node ir (Fig. 3a). Initially, node ir can be located relative to the first node by position vector $\boldsymbol{x}^{ir}$. The position vector contains not only an x and z component but also has a third empty component that allows it to interact with the displacement vector of the node, which has three degrees of freedom: two translational and one rotational. When the element rotates about the first node by angle ϕ, its new position relative to the first node can be expressed by an orthogonal transformation matrix as $\mathbf{T}_1^T\boldsymbol{x}^{ir}$, where

$$\mathbf{T}_1 = \begin{bmatrix} c & s & 0 \\ -s & c & 0 \\ 0 & 0 & 1 \end{bmatrix} \tag{7}$$

and s and c denote the sine and cosine of the angle ϕ. Therefore, displacement vector $\boldsymbol{q}_r^{ir}$ of node ir due to rigid body rotation can be expressed as

$$\boldsymbol{q}_r^{ir} = (\mathbf{T}_1^T - \mathbf{I})\boldsymbol{x}^{ir} \tag{8}$$

Translating this to all nodes and combining with Eq. (4), the displacements due to rigid body rotation are

$$\boldsymbol{q}_{\text{rig}} = \boldsymbol{q}_t + (\mathbf{T}^T - \mathbf{I})\boldsymbol{X} \tag{9}$$

where

$$\mathbf{T} = \begin{bmatrix} \mathbf{T}_1 & & 0 \\ & \ddots & \\ 0 & & \mathbf{T}_1 \end{bmatrix} \tag{10}$$

and vector $\boldsymbol{X}$ is simply a collection of the initial x and z coordiantes of the nodes and is defined explicitly as

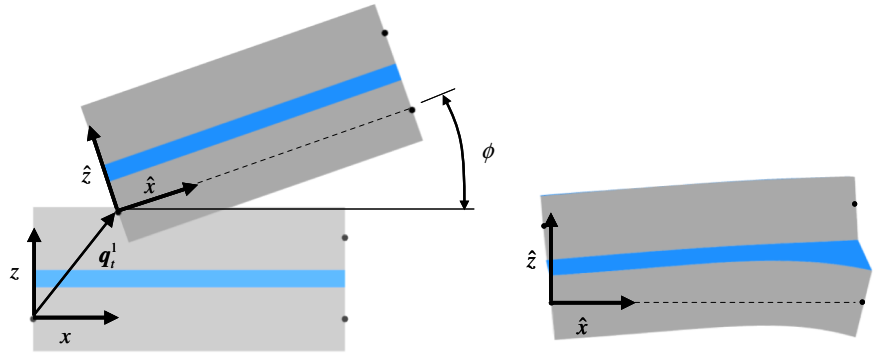

a) b)

Fig. 2 The nodal displacements broken up into two parts: a) rigid translation and rotations and b) local deformations.

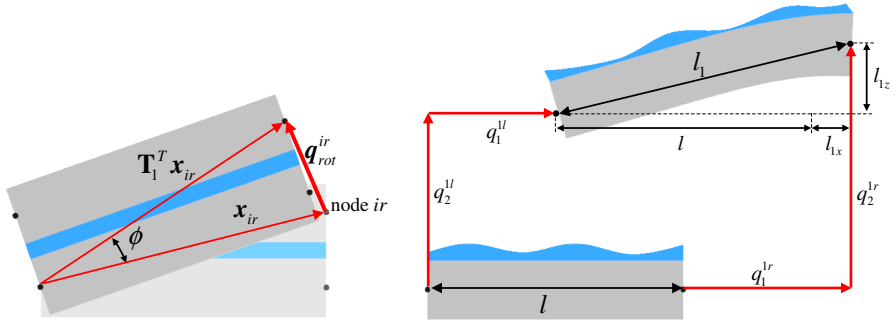

a) b)

Fig. 3 Displacements a) $\boldsymbol{q}_r^{ir}$ of node ir due to a rigid body rotation of the joint element and b) initial and current lengths of the first adherend, which are used to determine the rotation angle.

$$\boldsymbol{X} = [\,\boldsymbol{X}^{1l} \quad \boldsymbol{X}^{1r} \quad \ldots \quad \boldsymbol{X}^{il} \quad \boldsymbol{X}^{ir} \quad \ldots \quad \boldsymbol{X}^{Nl} \quad \boldsymbol{X}^{Nr}\,]^T \tag{11}$$

where the first superscript identifies the plate number and the following letter, either l or r, refers to the left or right node, respectively. The nodal coordinate vector for the ith adherend and the left node is defined as

$$\boldsymbol{X}^{il} = [\,x^{il} \quad z^{il} \quad 0\,] \tag{12}$$

whereas the coordinate vector of the right node is defined in an identical fashion.

2. Determination of the Rotation Angle

If the rotation is not constant within the joint, the rotation angle is an approximation. Adhering to the conventional approach for corotational beam formulations, the rotation angle was chosen to be the rotation of the first adherend as shown in Fig. 3a. To find the transformation matrix of Eq. (7), the sine and cosine of the rotation angle can be expressed as

$$s = \sin\phi = \frac{l_{1z}}{l_1} \tag{13}$$

and

$$c = \cos\phi = \frac{l_{1x}}{l_1} \tag{14}$$

which are defined in terms of the nodal displacements of the first adherend by

$$l_{1x} = l + q_1^{1r} - q_1^{1l}, \quad l_{1z} = q_2^{1r} - q_2^{1l} \tag{15}$$

where l is the original length of the element and l_1, l_{1x}, and l_{1z} refer to the current length of the first adherend and the length decomposed into x and z components (Fig. 3b).

3. Local Coordinate System

Here, the internal force vector and stiffness matrix will be found in the local rotating coordinate system. The stress and strain of the adherends and adhesive are assembled together in one stress and one strain vector as shown:

$$\hat{\boldsymbol{\sigma}} = [\,\hat{\boldsymbol{\sigma}}_1 \quad \hat{\boldsymbol{\sigma}}_{a1} \quad \ldots \quad \hat{\boldsymbol{\sigma}}_i \quad \hat{\boldsymbol{\sigma}}_{ai} \quad \ldots \quad \hat{\boldsymbol{\sigma}}_{N-1} \quad \hat{\boldsymbol{\sigma}}_{a(N-1)} \quad \hat{\boldsymbol{\sigma}}_N\,]^T \tag{16}$$

and

$$\hat{\boldsymbol{\varepsilon}} = [\,\hat{\boldsymbol{\varepsilon}}_1 \quad \hat{\boldsymbol{\varepsilon}}_{a1} \quad \ldots \quad \hat{\boldsymbol{\varepsilon}}_i \quad \hat{\boldsymbol{\varepsilon}}_{ai} \quad \ldots \quad \hat{\boldsymbol{\varepsilon}}_{N-1} \quad \hat{\boldsymbol{\varepsilon}}_{a(N-1)} \quad \hat{\boldsymbol{\varepsilon}}_N\,]^T \tag{17}$$

where the overbar caret denotes quantities in the local rotating coordinate system. The local stress and strain vectors for the ith adherend, $\hat{\boldsymbol{\sigma}}_i$ and $\hat{\boldsymbol{\varepsilon}}_i$, contain only the axial compenents of stress and strain in the x direction, $\hat{\sigma}_i$ and $\hat{\varepsilon}_i$. The local stress and strain vectors for the ith adhesive, $\hat{\boldsymbol{\sigma}}_{ai}$ and $\hat{\boldsymbol{\varepsilon}}_{ai}$, contain peel and shear compenents of the stress, $\hat{\sigma}_{ai}$ and $\hat{\tau}_{ai}$, and the strain, $\hat{\varepsilon}_{ai}$ and $\hat{\gamma}_{ai}$. Using beam theory and assuming small strains in the rotated coordinate system, the strains are related to the adherend centerline displacements, $\hat{\boldsymbol{u}}$, by the equation

$$\hat{\boldsymbol{\varepsilon}} = \mathbf{G}\hat{\boldsymbol{u}} \tag{18}$$

where the adherend centerline displacements are a collection of centerline displacement vectors for each adherend layer given as

$$\boldsymbol{u} = [\,\boldsymbol{u}_1^T \quad \ldots \quad \boldsymbol{u}_i^T \quad \ldots \quad \boldsymbol{u}_N^T\,]^T \tag{19}$$

and the centerline displacement vector of adherend i is given as

$$\boldsymbol{u}_i = [\,u_i(\hat{x}) \quad u_i(\hat{x})_{,\hat{x}} \quad w_i(\hat{x}) \quad w_i(\hat{x})_{,\hat{x}} \quad w_i(\hat{x})_{,\hat{x}\hat{x}} \quad w_i(\hat{x})_{,\hat{x}\hat{x}\hat{x}}\,]^T \tag{20}$$

where u and w are $\hat{x}$ and $\hat{z}$ direction displacements of the adherend centerline and subscript, $\hat{x}$ denotes the derivative with respect to $\hat{x}$. Additionally, $\mathbf{G}$ is an assembly of the contributions of the adherend and adhesive layers assembled in the form

$$\mathbf{G} = \begin{bmatrix} [\mathbf{G}_1] & & & & & & & \\ [\mathbf{G}_{a1}] & & & & & & & \\ & \ddots & & & & & & \\ & & [\mathbf{G}_i] & & & & & \\ & & [\mathbf{G}_{ai}] & & & & & \\ & & & \ddots & & & & \\ & & & & [\mathbf{G}_{N-1}] & & & \\ & & & & [\mathbf{G}_{a(N-1)}] & & & \\ & & & & & [\mathbf{G}_N] & & \end{bmatrix} \tag{21}$$

where the submatrices are defined as

$$\mathbf{G}_i = \begin{bmatrix} 0 & 1 & 0 & 0 & -\hat{z}_i & 0 \\ 0 & 0 & 0 & 0 & 0 & 0 \end{bmatrix} \tag{22}$$

and

$$\mathbf{G}_{ai} = \begin{bmatrix} 0 & 0 & \frac{1}{\eta_{ai}} & 0 & 0 & 0 & 0 & 0 & \frac{-1}{\eta_{ai}} & 0 & 0 & 0 \\ \frac{1}{\eta_{ai}} & 0 & 0 & \frac{t_i}{2\eta_{ai}} & 0 & 0 & \frac{-1}{\eta_{ai}} & 0 & 0 & \frac{-t_{i+1}}{2\eta_{ai}} & 0 & 0 \\ 0 & 0 & 0 & 0 & 0 & 0 & 0 & 0 & 0 & 0 & 0 & 0 \end{bmatrix} \tag{23}$$

with the thicknesses t_i and η_{ai} defined in Fig. 1a. All other terms in $\mathbf{G}$ are zero. Shape functions $\mathbf{N}$ derived for the linearly elastic case are used [8–10], and, assuming the deflections in the local coordinate system to be small, the local strains and displacements in the rotated coordinate system are related by the equation

$$\hat{\boldsymbol{\varepsilon}} = \mathbf{B}\hat{\boldsymbol{q}} \tag{24}$$

where $\mathbf{B}$ is defined as

$$\mathbf{B} = \mathbf{G}\mathbf{N} \tag{25}$$

The principle of virtual work of the element can be written as

$$\delta(W^{\text{Int}} - W^{\text{Ext}}) = 0 \tag{26}$$

and the internal work can be written as the internal nodal forces multiplied by the nodal virtual displacements:

$$\delta W^{\text{Int}} = \delta\hat{\boldsymbol{q}}^T\hat{\boldsymbol{f}}^{\text{Int}} \tag{27}$$

Because the deformations are small relative to the rigid body displacements, the internal virtual work can be rewritten as

$$\delta W^{\text{Int}} = \int_V \delta\hat{\boldsymbol{q}}^T\mathbf{B}^T\hat{\boldsymbol{\sigma}}\,\mathrm{d}V \tag{28}$$

Assuming that external forces only occur as nodal forces and moments, the external virtual work of the element becomes

$$\delta W^{\text{Ext}} = \delta\hat{\boldsymbol{q}}^T\hat{\boldsymbol{f}}^{\text{Ext}} \tag{29}$$

Finally, using Eq. (26), and noting the fact that the virtual displacements are arbitrary, the resulting equilibrium equation is

$$\int_V \mathbf{B}^T\hat{\boldsymbol{\sigma}}\,\mathrm{d}V = \hat{\boldsymbol{f}}^{\text{Ext}} \tag{30}$$

Now, the local internal nodal forces are

$$\hat{\boldsymbol{f}}^{\text{Int}} = \int_V \mathbf{B}^T \hat{\boldsymbol{\sigma}}\, \mathrm{d}V \tag{31}$$

with the local stiffness matrix being given by

$$\hat{\mathbf{k}} = \int_V \mathbf{B}^T \mathbf{D}\mathbf{B}\, \mathrm{d}V \tag{32}$$

where the material tangent stiffness matrix, $\mathbf{D}$, is given as

$$\mathbf{D} = \frac{\mathrm{d}\hat{\boldsymbol{\sigma}}}{\mathrm{d}\hat{\boldsymbol{\varepsilon}}} \tag{33}$$

Note that for linear elastic materials a reduced equation results requiring only integration in x, which can be carried out analytically.

4. Global Coordinate System

Now we seek to find the residual and the stiffness matrix in the global coordinate system. Because the internal work is not dependent on the frame of reference, one can write

$$\delta \boldsymbol{q}^T \boldsymbol{f}^{\text{Int}} = \delta \hat{\boldsymbol{q}}^T \hat{\boldsymbol{f}}^{\text{Int}} \tag{34}$$

where the nodal virtual displacements in the global frame are related to those in the local rotated coordinate frame through the equation

$$\delta \boldsymbol{q} = \delta \boldsymbol{q}_{\text{rig}} + \mathbf{T}\delta \hat{\boldsymbol{q}} \tag{35}$$

making Eq. (34)

$$\delta \boldsymbol{q}^T \boldsymbol{f}^{\text{Int}} = (\delta \boldsymbol{q}^T - \delta \boldsymbol{q}_{\text{rig}}^T)\mathbf{T}\hat{\boldsymbol{f}}^{\text{Int}} \tag{36}$$

Because rigid body motion does not result in the generation of internal forces,

$$\delta \boldsymbol{q}_{\text{rig}}^T \mathbf{T}\hat{\boldsymbol{f}}^{\text{Int}} = 0 \tag{37}$$

and Eq. (36) becomes

$$\delta \boldsymbol{q}^T \boldsymbol{f}^{\text{Int}} = \delta \boldsymbol{q}^T \mathbf{T}\hat{\boldsymbol{f}}^{\text{Int}} \tag{38}$$

With the virtual displacements being arbitrary, the internal nodal force vector in the global coordinate system becomes

$$\boldsymbol{f}^{\text{Int}} = \mathbf{T}\hat{\boldsymbol{f}}^{\text{Int}} \tag{39}$$

To find the global tangent stiffness matrix, differentiation of Eq. (39) gives

$$\delta \boldsymbol{f}^{\text{Int}} = \delta\mathbf{T}\hat{\boldsymbol{f}}^{\text{Int}} + \mathbf{T}\delta \hat{\boldsymbol{f}}^{\text{Int}} \tag{40}$$

The second term in the preceding equation can be written as

$$\mathbf{T}\delta \hat{\boldsymbol{f}}^{\text{Int}} = \mathbf{T}\mathbf{k}\delta \hat{\boldsymbol{q}} = \mathbf{T}\hat{\mathbf{k}}\mathbf{T}^T\delta \boldsymbol{q} - \mathbf{T}\hat{\mathbf{k}}\mathbf{T}^T\delta \boldsymbol{q}_{\text{rig}} \tag{41}$$

The last term vanishes, because, as before, displacements resulting in rigid body translation and rotation do not generate any internal force. The first term on the right side of Eq. (40) is more difficult to obtain. The difficulty lies in the fact that $\mathbf{T}$ contains sines and cosines of ϕ, which in turn contain $\boldsymbol{q}^1$ and l. However, Crisfield [16] provides an approximation, which assumes that the extension δl is small. Based on this assumption, the first term in Eq. (40) can be rewritten as

$$\delta\mathbf{T}\hat{\boldsymbol{f}}^{\text{Int}} = \mathbf{T}_{,\phi}\hat{\boldsymbol{f}}^{\text{Int}}\phi_{,\boldsymbol{q}}\delta \boldsymbol{q} \tag{42}$$

where

$$\mathbf{T}_{,\phi} = \begin{bmatrix} \mathbf{T}_{1,\phi} & & 0 \\ & \ddots & \\ 0 & & \mathbf{T}_{1,\phi} \end{bmatrix} \tag{43}$$

and

$$\mathbf{T}_{1,\phi} = \begin{bmatrix} -s & c & 0 \\ -c & -s & 0 \\ 0 & 0 & 0 \end{bmatrix} \tag{44}$$

Similarly,

$$\phi_{,\boldsymbol{q}} = [\phi_{1,\boldsymbol{q}} \quad 0 \quad \ldots \quad 0] \tag{45}$$

and

$$\phi_{1,\boldsymbol{q}} = \frac{1}{l_1}[s \quad -c \quad 0 \quad -s \quad c \quad 0] \tag{46}$$

Combining all of these equations, the global tangent stiffness matrix can be written as a combination of material stiffness $\mathbf{k}_{\text{mat}}$ and geometric stiffness $\mathbf{k}_{\text{geo}}$, in the relation

$$\mathbf{k} = \mathbf{k}_{\text{mat}} + \mathbf{k}_{\text{geo}} \tag{47}$$

where

$$\mathbf{k}_{\text{geo}} = \mathbf{T}_{,\phi}^T \hat{\boldsymbol{f}}^{\text{Int}} \phi_{,\boldsymbol{q}} \tag{48}$$

and

$$\mathbf{k}_{\text{mat}} = \mathbf{T}\hat{\mathbf{k}}\mathbf{T}^T \tag{49}$$

Both the geometric and material stiffness matrices are functions of the nodal displacements, making the system of equilibrium equations nonlinear. The Newton–Raphson method can be used to find the solution. It was already noted that one of the benefits of this method is that the formulation of the linear element, introduced previously [9], can be used. If the materials involved are linearly elastic, the local rotational frame stiffness is not a function of the nodal displacements. Because numerical integration is used in finding these vectors/matrices, the integration must only be carried out once during the analysis. This saves a considerable amount of computational time, especially for an element like the joint element, which requires more refined integration for the higher order shape functions.

B. Material Nonlinearities

Because modern polymeric adhesives often display highly nonlinear material behavior before joint failure, it is necessary to include material nonlinearities in the joint element to estimate joint strengths more correctly. A particularly simple nonlinear elastic stress law was chosen:

$$\hat{\boldsymbol{\sigma}} = \hat{\boldsymbol{\sigma}}(\hat{\boldsymbol{\varepsilon}}) \tag{50}$$

where the stress is some general function of the strain. The only major change from the previous corotational formulation is that Eq. (31) becomes

$$\hat{\mathbf{k}} = \int_V \mathbf{B}^T \mathbf{D}(\hat{\boldsymbol{q}})\mathbf{B}\, \mathrm{d}V \tag{51}$$

where the local stiffness matrix in the rotated coordinate system is now a function of the local displacements.

Although it would be more correct to use an incremental flow-type plasticity formulation that distinguishes loading and unloading stiffness and which takes account of path dependency, the simple nonlinear elastic relation, which assumes no permanent plastic strain,

was chosen for several reasons. The joint element is meant to be a design tool to give general approximations, and so it is not expected that such a tool will be used in situations requiring unloading capabilities. Additionally, the nature of adhesively bonded joints is such that the highest stresses occur as concentrations near the joint edges. Because the failing adhesive domain is eliminated in the iteration process (to be described later) the assumption of a nonlinear elastic-type stress-strain law before adhesive failure suffices for this modeling process because potential regions of "unloading" are minimal [17]. Thus, this assumption does lead to a meaningful rendition of the joint physics yet facilitates an efficient (in the computational sense) solution strategy.

One other aspect worthy of note is the integration requirements for the nonlinear material formulation. When the adherends have a nonlinear stress-strain relationship, Eqs. (31) and (51) must be integrated over $\hat{x}$ and $\hat{z}$ at each Newton–Raphson iteration to allow a general stress-strain relationship. This causes a considerable increase in computational time. However, there are some cases in which this is not necessary. If only the adhesive layers have a nonlinear stress-strain relation, integration over $\hat{z}$ can be avoided because the stress is constant through the thickness of the adhesive layer. Additionally, if the functions for the nonlinear stress-strain relations are known (and simple enough), integration over $\hat{z}$ can be accomplished analytically. However, this would mean that the formulation is only good for that specific stress-strain relation and cannot be extended to other general relations.

C. Adhesive Crack Growth

To accommodate adhesive failure, when some user defined failure criterion is reached in some part of the adhesive layer, that portion of the adhesive is considered "failed" and can carry no load and has no stiffness. Setting the stress and stiffness of that portion of the adhesive to zero is an easy way to model the failure of the adhesive, but the shape functions for the joint element were not originally calculated based on a joint with failed adhesive and cannot accurately model this new situation. Therefore, as with more traditional shape function prescribed FEs, more elements are required to accurately find the solution. In the case of failed adhesive, a greater number of elements may be needed, as will be illustrated later.

To increase the accuracy of the joint element after adhesive failure and crack growth, a method of removing the adhesive and adapting the mesh to the cracked and uncracked portions was devised. Because the joint element is meant to be used as a user defined element in a larger global assembly in commercially available FE software, the mesh change would have to be strictly internal to the element so that the surrounding model does not have to change. Therefore, a subassembly method was devised to handle adhesive failure (Fig. 4) and is outlined in Fig. 5.

First, when failure in the adhesive is detected, the element is replaced by a subassembly with three elements as shown in Fig. 4b. The length of the crack determines the lengths of the subassembly elements. Within a Newton–Raphson-type solver, the nodal displacements are prescribed (guessed) and the stiffness and internal

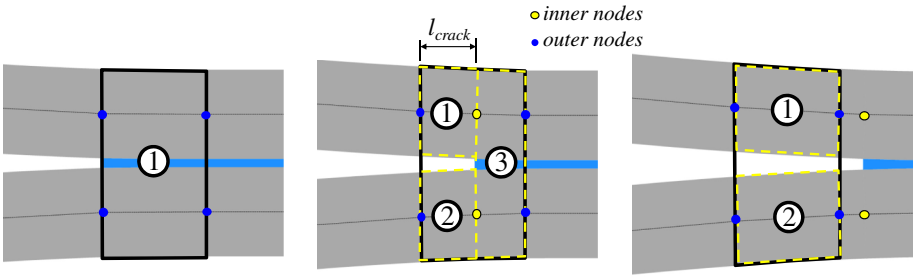

a) Uncracked **b) Partially cracked** **c) Fully cracked**

Fig. 4 Diagram showing a) an uncracked joint element, b) a partially cracked element, and c) a fully cracked joint element.

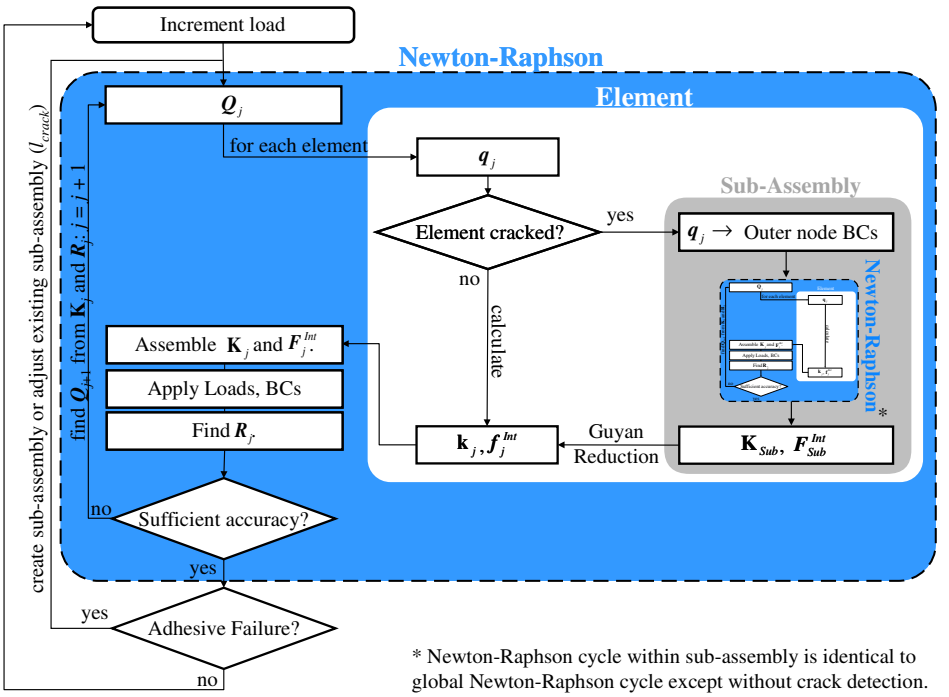

* Newton-Raphson cycle within sub-assembly is identical to global Newton-Raphson cycle except without crack detection.

Fig. 5 Flow chart showing how a cracked element subassembly is incorporated into a joint element solution procedure.

force vector for the element are calculated. These vectors/matrices for all of the elements in the assembly are assembled, boundary conditions and loads are applied, and the residual (error of the initial nodal displacement guess) is calculated. If the residual is outside some tolerance, a new nodal displacement "guess" is calculated based on the previous displacement, residual, and stiffness values and the whole cycle repeats.

In the case of a joint element with failed adhesive, only the outer nodal displacements are prescribed because the global FE assembly is not aware of the existence of the subassembly and the inner nodes. Therefore, the subassembly becomes a nonlinear model within another nonlinear model and must be solved with its own Newton–Raphson-type solution procedure. The prescribed nodal displacements of the outer nodes become the boundary conditions for the subassembly, and the whole system is solved using a nonlinear solver. When the desired error tolerance is reached, a stiffness matrix and internal force vector for the subassembly has been calculated. However, these quantities still have the inner degrees of freedom contained within. The force vector and stiffness matrix are then reduced using the Guyan reduction method [18–20]. Once the internal degrees of freedom are removed, the stiffness matrix and force vector can be considered to be that of the equivalent joint element and can be passed onto the global assembly.

After the global system is solved, there is a check to see if the crack has grown or if new adhesive failure has been detected. If this is the case, the subassembly is adjusted by changing the lengths of the subassembly elements, and the global system is re-solved. This is done until no new adhesive failure occurs and the crack is in equilibrium. A crack scaling constant, C_1, has been introduced to speed up or slow down crack growth as needed and is used in the equation

$$l^{\text{cur}}_{\text{crack}} = l^{\text{cur}}_{\text{crack}} - C_1(l^{\text{cur}}_{\text{crack}} - l^{\text{prev}}_{\text{crack}}) \tag{52}$$

where $l^{\text{prev}}_{\text{crack}}$ is the previous crack length (before the global Newton–Raphson procedure) and $l^{\text{cur}}_{\text{crack}}$ is the current crack length. Setting $C_1 < 0$ causes the crack to grow further than detected, which is useful when multiple iterations are needed to find crack equilibrium. Setting $C_1 > 0$ causes the crack to grow less than detected, which is necessary when crack overshoot is a concern.

The advantage of this method is that fewer elements are needed in order to capture accurately crack growth. One can use the minimum number of elements needed to capture accurately the material and geometric nonlinear effects without crack growth being a factor. This can dramatically reduce the number of elements required, especially when there is little material nonlinearity and when strains in the joint are small.

One of the major disadvantages of this method is the increased computational time. A local nonlinear problem must be solved within each iteration of the global nonlinear problem. Although the local nonlinear problem is always limited to three elements, it can significantly increase the runtime. Furthermore, the global load increment is repeated if the crack grows and the subassemblies need to be created or remeshed. Although the crack scaling parameter can significantly help in limiting the iterations needed to find crack equilibrium, this process can still be costly. However, the costs can be justified if joint strength prediction is of concern. One must decide how much fidelity versus efficiency is required for the problem at hand and choose a model accordingly.

D. Adhesive Model Characterization

One of the most important inputs for determining the strength of a joint is the characterized adhesive constitutive response. There have been many methods of characterizing the adhesive material, but two have emerged as the most common: bulk adhesive tensile test and fracture mechanics characterization tests (double cantilever beam, end notched flexure, etc.). Therefore, the following sections outline methods of using both bulk adhesive tensile test data and fracture mechanics inputs to characterize the joint adhesive. Ultimately, the test data available and personal preferences will decide which route to take.

1. *Bulk Adhesive Tensile Characterization*

One common way of characterizing adhesive materials is by performing tensile tests on bulk adhesive specimens, such as those depicted in Fig. 6. The joint element was originally intended for fracture mechanics characterization with uncoupled peel and shear components (mode 1 and 2) as will be discussed in the next section. However, a method of uncoupling the shear and normal responses based on bulk adhesive data has been derived and will be presented here. This method requires more assumptions and is much more restrictive than coupled equivalent stress and strain methods [5,12,21], but was chosen to adapt the fracture mechanics model to bulk adhesive data without additional programming. Future improvements on the model will include the adoption of more accurate adhesive models.

If the adhesive is much deeper than it is thick ($b_{ai} \gg \eta_{ai}$), it can be considered to be in a state of plane strain in the z–x plane (Fig. 7), and the stress-strain relation for plane strain can be applied. Furthermore, if we assume that the adhesive is perfectly bonded to the adherends and that the adherends are much stiffer than the adhesive ($E_{ai} \ll E_i$), then it can be argued that the extensional strain in the adhesive is much smaller than the peel and shear components ($\hat{\varepsilon}_{xai} \ll \hat{\varepsilon}_{ai}, \hat{\gamma}_{ai}$), which is the root of the assumption

$$\hat{\varepsilon}_{xai} \approx 0 \tag{53}$$

This assumption gives rise to the common practice in adhesive joint analysis of ignoring the extensional stress and strain in the formulation. With the extensional strains being relatively small, the strain energy of the adhesive layer is virtually unaffected when the extensional strain is ignored. However, the extensional stress (in both the x and y directions) is not insignificant, placing the adhesive in a state of triaxial stress [22]. Using these assumptions and linear elasticity, the extensional stress in the adhesive, $\hat{\sigma}_{xai}$, can be written in terms of the peel strain:

$$\hat{\sigma}_{xai} = C_2 \nu_{ai} \hat{\varepsilon}_{ai} \tag{54}$$

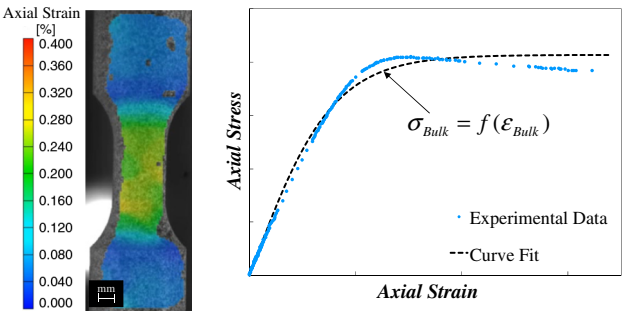

a) b)

Fig. 6 Adhesive characterized by a) experimental bulk adhesive tensile tests, then b) fitting a curve (in this case the tanh function) to the stress-strain plot [17].

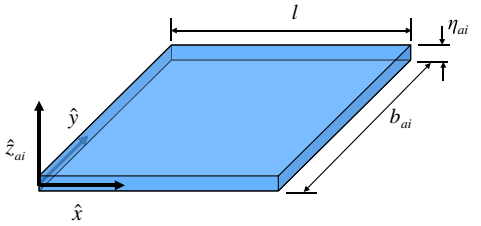

Fig. 7 Assuming that the adhesive is perfectly bonded to the adherends, the adhesive here considered a constrained body under triaxial stress [17].

where

$$C_2 = \frac{E_{ai}}{(1+\nu_{ai})(1-2\nu_{ai})} \tag{55}$$

and where E_{ai} and ν_{ai} are the Young's modulus and Poisson's ratio of the ith adhesive layer. The axial adhesive stress can be written in terms of the peel stress:

$$\hat{\sigma}_{xai} = \frac{\nu_{ai}}{1-\nu_{ai}}\hat{\sigma}_{ai} \tag{56}$$

The same relation is true for the extensional stress in the y direction, $\hat{\sigma}_{yai}$. This can be used to find the extensional stress without necessarily including it into the formulation. Furthermore, the peel stress becomes a function of the peel strain only [17]:

$$\hat{\sigma}_{ai} = \frac{1-\nu_{ai}}{(1-2\nu_{ai})(1+\nu_{ai})}E_{ai}\hat{\varepsilon}_{ai} \tag{57}$$

This shows that the effective "resistance" to deformation in the z direction is amplified by a factor that depends on Poisson's ratio. Although this relation is intended for linear elasticity, the relation was assumed to hold for the nonlinear stress-strain relation as well. Therefore, the stress-strain relation was redefined as [17]

$$\hat{\sigma}_{ai} = \frac{1-\nu_{ai}}{(1-2\nu_{ai})(1+\nu_{ai})}f(\hat{\varepsilon}_{ai}) \tag{58}$$

and the effective modulus is increased by the consideration of a triaxial stress state.

A von Mises failure criterion was chosen for this particular formulation, although the same formulation could easily be altered for a different threshold criterion [23]. Applying the notation for the adhesive layer, assuming the shear stresses in the x–y and y–z planes to be negligible, and using Eq. (56), the von Mises equivalent stress in terms of the shear and peel stress components is

$$\sigma_{\text{vm}}^2 = \left(\frac{1-2\nu_{ai}}{1-\nu_{ai}}\right)^2\sigma_{ai}^2 + 3\tau_{ai}^2 \tag{59}$$

Although the von Mises equivalent stress is normally used to find the yield stress, in this case it will be assumed to hold for the entire nonlinear adhesive stress/strain response. Therefore, the von Mises equivalent stress for a certain adhesive will be a nonlinear function of the adhesive strain found using bulk adhesive tensile tests (Fig. 6a):

$$\sigma_{\text{vm}} = \sigma_{\text{Bulk}} = f(\varepsilon_{\text{Bulk}}) \tag{60}$$

The function describing the stress can be either a functional or simply tabular data from material testing. To use this data in the current formulation with uncoupled peel and shear modes, the ratio of peel to shear stress must be defined for the problem. A new variable will be introduced, ψ_i, which represents the ratio of peel to shear stress for adhesive layer i of a particular joint configuration:

$$\psi_i = \frac{\hat{\sigma}_{ai}}{|\hat{\tau}_{ai}|} \tag{61}$$

allowing the shear stress to be defined as a function of the bulk stress:

$$\hat{\tau}_{ai}^2 = \frac{\sigma_{\text{Bulk}}^2}{3 + (\frac{1-2\nu_{ai}}{1-\nu_{ai}})^2\psi_i^2} \tag{62}$$

The method of finding the strain was a bit more arbitrary. Others have done this by using a von Mises strain criterion or similar methods [5,12,21]. For the current formulation, it was assumed that the bulk adhesive tensile specimen strain and the adhesive layer strains were linearly related to each other through the equations

$$\hat{\gamma}_{ai} = C_3\varepsilon_{\text{Bulk}} \tag{63}$$

and

$$\hat{\varepsilon}_{ai} = C_4\varepsilon_{\text{Bulk}} \tag{64}$$

where constants C_3 and C_4 are found such that the initial slopes of the shear and peel stress-strain curves become the normal and shear modulus, respectively.

For an actual joint, the ratio of peel to shear stress, ψ_i, not only varies across the joint but changes during loading due to nonlinear geometric effects and nonlinear material effects. Therefore, this value will in actuality be a function of the joint geometry, loading, materials, and location within the adhesive in question. However, to simplify the determination of this value, it is proposed that one assume that the ratio of peel to shear does not change significantly during the loading event and that only the stress at ends of the joint where the stress concentrations reside is important. The impact of this first assumption will be assessed later. Therefore, this value can be approximated by taking the ratio of the maximum peel to shear stress of the linearly elastic case as illustrated in Fig. 8.

For balanced joints with the same adherend materials and geometries, the maximum occurs on both ends of the adhesive and is identical on either end. However, for unbalanced joints, the stress concentrations at the ends of the adhesive can be of unequal magnitude. Finding the peel to shear ratio based on the higher and lower of the two stress concentrations can provide a good upper and lower bound to the nonlinear solution.

To approximate the von Mises failure criterion for uncoupled shear and peel, an uncoupled strain-based criterion was chosen that simply considered the adhesive failed when

$$\frac{\hat{\varepsilon}_{ai}}{\varepsilon_c} = 1 \quad \text{or} \quad \frac{\hat{\gamma}_{ai}}{\gamma_c} = 1 \tag{65}$$

where ε_c and γ_c are critical peel and shear strain values. These values are found by applying Eqs. (63) and (64) to the maximum strain of the bulk adhesive tensile test data.

Though it might seem unusual to use a strain-based criterion to approximate the von Mises stress, it should be kept in mind that a von Mises yield criterion was already applied to get from the bulk adhesive tensile test data to the peel and shear stress-strain relations. If the peel to shear ratio, ψ_i, was chosen correctly, both the shear and peel components should be close to their respective critical values at the same time.

2. *Fracture Mechanics Characterization*

The joint element adhesive model is very similar to the CZM [11,24–27] and is inherently suited for fracture mechanics-type inputs. One of the main differences between many mainstream CZMs and the joint element adhesive model lies in the thickness of the cohesive zone. Many CZMs have no thickness and lie at the interface between continuum elements. Because it has no thickness, a traction-

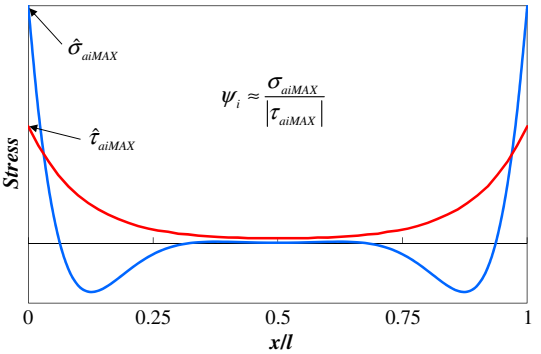

Fig. 8 The peel to shear ratio for adhesive i approximated by dividing the maximum peel stress by the maximum shear stress for the linear elastic adhesive case.

separation law rather than a stress-strain law is defined for the CZM. Thus, cracks in the center of the adhesive layer can be differentiated from cracks at the interface by placing CZM elements at different locations within the adhesive, although this is computationally very costly. The joint element, on the other hand, resembles a cohesive zone with an explicit thickness. The entire adhesive layer is a single cohesive zone, and cracks in the middle of the adhesive are not differentiated from those at the interface. The traction-separation law can be transferred approximately to a stress-strain law by dividing the separation by the thickness as shown in Fig. 9. Although no examples are presented in the present study using such characterization, this brief discussion illustrates the procedure.

For this type of adhesive characterization, the shear and peel responses are isolated and characterized in a series of experiments [28]. The peel and shear responses are considered to be uncoupled and depend solely on the vertical and horizontal separations of the adherends, respectively. Typically, a critical stress and fracture toughness is identified for mode 1 and mode 2. Because the joint element model does not have continuum elements to represent the adhesive, it is recommended that the initial slopes of the stress-strain laws be set to the elastic modulus for peel and shear.

Finally, adhesive failure can be defined as occurring when

$$\left(\frac{G_1}{G_{1C}}\right)^i + \left(\frac{G_2}{G_{2C}}\right)^j = 1 \tag{66}$$

The values of i and j can be chosen based on the preference of the element user.

III. Results and Validation

A. Geometric Nonlinearities

To verify the corotational formulation, several example joint configurations were analyzed using the joint element and compared with two-dimensional (2-D) dense mesh FE solutions with nonlinear geometric effects to demonstrate the joint element's ability to capture large rotation situations and to show how many elements are typically required.

The first example was an unbalanced single overlap joint, using the joint elements with a single adhesive layer and two adherends. The unbalanced single lap joint illustrated in Fig. 10 was loaded in a displacement-controlled tension. The adherends were titanium ($E = 110$ GPa, $\nu = 0.33$) and aluminum ($E = 70$ GPa, $\nu = 0.33$), with EA 9394 as the adhesive layer ($E = 4$ GPa, $G = 1.79$ GPa). As before, the shallow width of the joint required the use of a plane stress joint element formulation and the use of 2-D plane stress elements for the dense 2-D FE mesh model. The joint element model had either one or 40 beam elements with one joint element, whereas 154,000 elements were used for the 2-D dense mesh model (Fig. 11a). Because the joint does not fail in this analysis, the results do not depend on the number of joint elements used. A comparison of the load-displacement plots of the different models is shown in Fig. 11b. The joint element model was able to replicate the response quite well, even with only one beam element rather than 40. The actual joint region requires fewer elements because all of the bending takes place outside of the overlap region. The increased flexural rigidity of the overlap region causes it to rotate rigidly rather than bend. Therefore, more elements are required outside the overlap regions to best capture the nonlinear geometric effects of the joint.

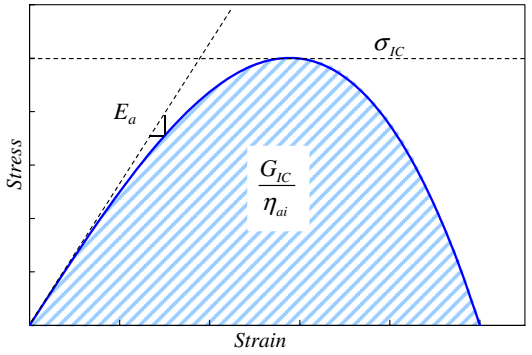

Fig. 9 Fracture mechanics properties such as critical stress and fracture toughness used to form an adhesive stress-strain law for the joint element.

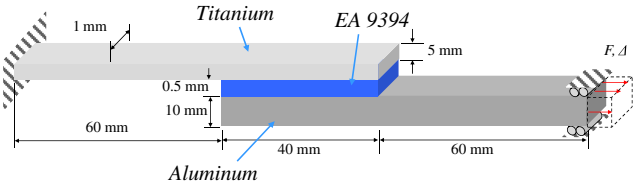

Fig. 10 Single lap joint used to validate joint element corotational formulation.

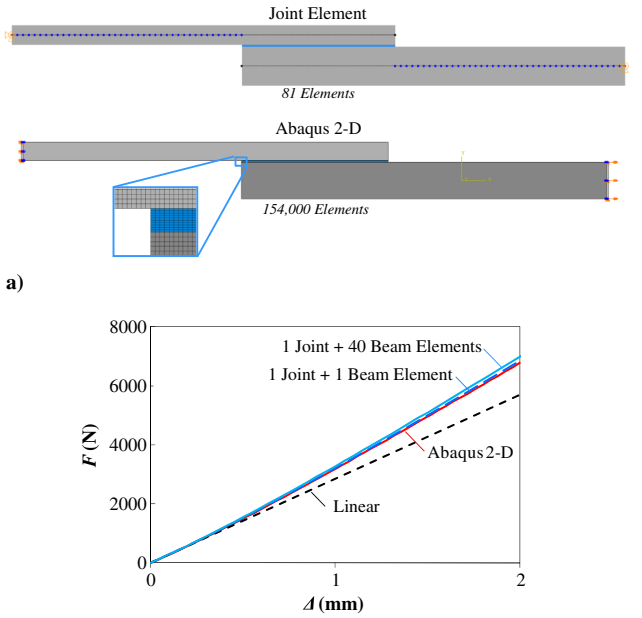

Fig. 11 Comparison of a) joint element and 2-D dense mesh FE representation of unbalanced single lap joint and b) the resulting load vs displacement plot.

B. Material Nonlinearities

The material nonlinearity examples featured in this section highlight adherend nonlinearity and adhesive nonlinearity separately to show the strengths and weaknesses. The limitations and abilities of the joint element in modeling nonlinear adherends are shared by beam elements in general, and more in-depth discussion on these limitations and how to overcome them is dealt with extensively in literature [29–36].

The example used to demonstrate adherend material nonlinearity is the single lap joint shown in Fig. 10, but with elastic perfectly plastic adherends. The yield stress for the titanium was set at 1050 MPa, the aluminum was at 300 MPa, and both the joint element and Abaqus 2-D models used the same material law. Large rotations were considered in the analysis, and the adhesive was given linear material properties to isolate the effect of nonlinear adherends. Figure 12a shows the load-displacement plot for the joint element model using different numbers of elements. As can be seen, the predictions of all models are relatively close, but more elements are certainly necessary for a converged solution. However, the load-displacement plot did not resemble that of the Abaqus 2-D dense mesh model shown in Fig. 12b. The load predicted by the 2-D dense mesh model drops after a peak, whereas the joint element model does not drop, but continues to hold more load. There are two factors that contribute to this. First, the beam model assumes that the displacement and strain vary linearly in the z direction. Because this is not the

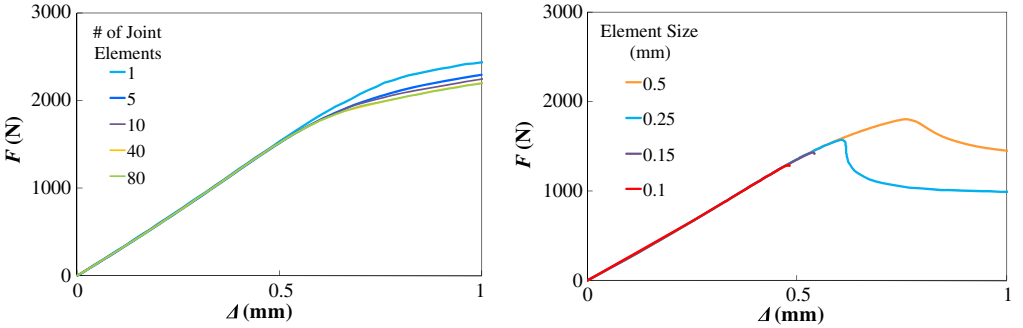

Fig. 12 Plots showing the effect of element size on the load-displacement response of the single lap joint featured in Fig. 10 with nonlinear adherends for the a) joint element and b) dense 2-D FE mesh.

case after yielding, the model is inaccurate after initial yielding and the softening is unable to localize. Second, because the stress-strain relation for the adherend is nonlinear elastic, unloading of the adherends is inaccurate. When the adherends first yield, the strain increases dramatically at one point (localization) whereas the rest of the adherend unloads. This causes inaccurate results after initial yielding of the adherends. A plastic hinge theory could improve this quality, as will be discussed later.

Another observation about the 2-D dense mesh FEM is that the solution continues to change when the element size is reduced. This is due to the stress singularity at the reentrant corners. As the element size is decreased, the stress concentration rises and the adherends yield sooner and more dramatically. Furthermore, the solution cuts off after the peak for an element size of 0.15 and 0.1 mm. This cutoff was due to the commercial FE analysis software, which ends the analysis after the step size has become too small. This may also be due to the stress singularity at the reentrant corners and illustrates some of the potential difficulties of modeling joints with dense continuum element meshes.

This example illustrates why one should avoid using the joint element when failure of the joint is dominated by adherend yielding. It also brings out the need of applying some of the measures adopted for beam elements to the joint element to better capture the material softening of the adherends.

The second example, illustrating nonlinear adhesive, is the same joint discussed previously, except with linear adherends and a nonlinear adhesive stress-strain relation. The adhesive had an elastic perfectly plastic bulk adhesive tensile test stress-strain relation, with the linear properties being that of EA 9394 ($E = 4$ GPa, $G = 1.5$ GPa) and the bulk yield stress being 40 MPa. The procedure outlined previously was followed to find the peel and shear yield stress, σ_{aY} and τ_{aY}. The adhesive was allowed to yield indefinitely so that no crack would form or grow. This is an upper-bound prediction of joint strength according to the global yielding criterion proposed by Crocombe [37].

Because the joint was unbalanced, two peel to shear ratios were found: one on each side of the adhesive. The left side was the side with the greatest magnitude of adhesive stress, whereas the right side was a bit lower. Because the adhesive can yield indefinitely, the maximum load will not be reached until both sides of the adhesive begin to yield. Therefore, it was expected that the peel to shear ratio of the right side, the last side to yield, would result in the most realistic solution. The peel to shear ratios and peel and shear yield stresses, along with predicted joint strengths, are shown in Table 1. A comparison of the load-displacement response using the peel to shear ratio from the left (high ratio) and the right (low ratio) is shown in Fig. 13a. This is expected to provide bounds for the solution.

Table 1 The peel to stress ratio for the considered unbalanced joint, which is different on each side and produces a different strength prediction

Side of adhesive	Stress concentration	ψ	σ_{aY}, MPa	τ_{aY}, MPa	Predicted strength, kN
Left	Higher	1.63	29.0	17.1	710
Right	Lower	1.04	21.3	20.5	819

The load-displacement plot for different element sizes using the 2-D dense mesh model is shown in Fig. 13b, whereas the same plot for different numbers of joint elements is shown in Fig. 13c. As with the nonlinear adherend solution (Fig. 12), the reentrant corners caused stress singularities, which cause the solution to be mesh dependent for the 2-D dense mesh model. However, it appears that, for the element sizes shown, the joint element predictions using the high and low peel to shear ratios provide an upper and lower bound for the 2-D dense mesh solution. For the joint element model, if there are not enough elements the adhesive does not reach yielding along the entire length of the adhesive. However, with enough elements, the yielding advances properly across the adhesive.

C. Crack Growth

To illustrate the benefits of growing a crack by remeshing rather than just setting the failed adhesive stiffness and stress to zero, a bilayered beam joint was pulled apart as shown in Fig. 14a. The joint was 5 mm wide, and the adherends had a stiffness of 100 GPa and Poisson's ratio of 0.33. The adhesive had a Young's modulus of 1 GPa and was linear up to failure, which occurred at 500 MPa (see Fig. 14b). The simplistic linear-until-failure adhesive was chosen because an analytical solution can be found and because it allows crack growth without material nonlinearity, isolating this aspect of the joint element.

Two different models were compared that show the benefits of remeshing. First, rather than removing the adhesive and remeshing, the stress and stiffness of the adhesive were simply set to zero when the stress reached 500 MPa. Second, the failed adhesive was removed and the element was replaced by a subassembly (i.e., remeshing) as illustrated in Fig. 4. The results of the two models with different ways of handling crack growth are shown in Fig. 15. The drawbacks to remeshing are discussed in Sec. II.D, and the benefits are clearly illustrated here. For the first model, the postpeak solution oscillates around the analytical solution with the oscillation amplitude reducing for more elements. The second model with the remeshing, on the other hand, is extremely close to the analytical solution with just a single element. There is some oscillation after the peak, but this is suspected to be caused by crack overshoot. This effect, however, disappears entirely with only four elements. This example dramatically shows that remeshing the element to represent crack growth can result in huge elemental savings over zeroing the adhesive stiffness.

D. Experimental Validation

Last, the joint element was validated via comparison with experimental data published by Harris and Adams [12] on single lap joints. The tests were carried out according to ASTM D1002-72 specifications. The geometric parameters are shown in Fig. 16. The adhesive was MY750, and three different aluminum alloys served as the adherends. The only difference between the alloys was the 0.2% proof stress, as shown in Table 2. The adherends were modeled with

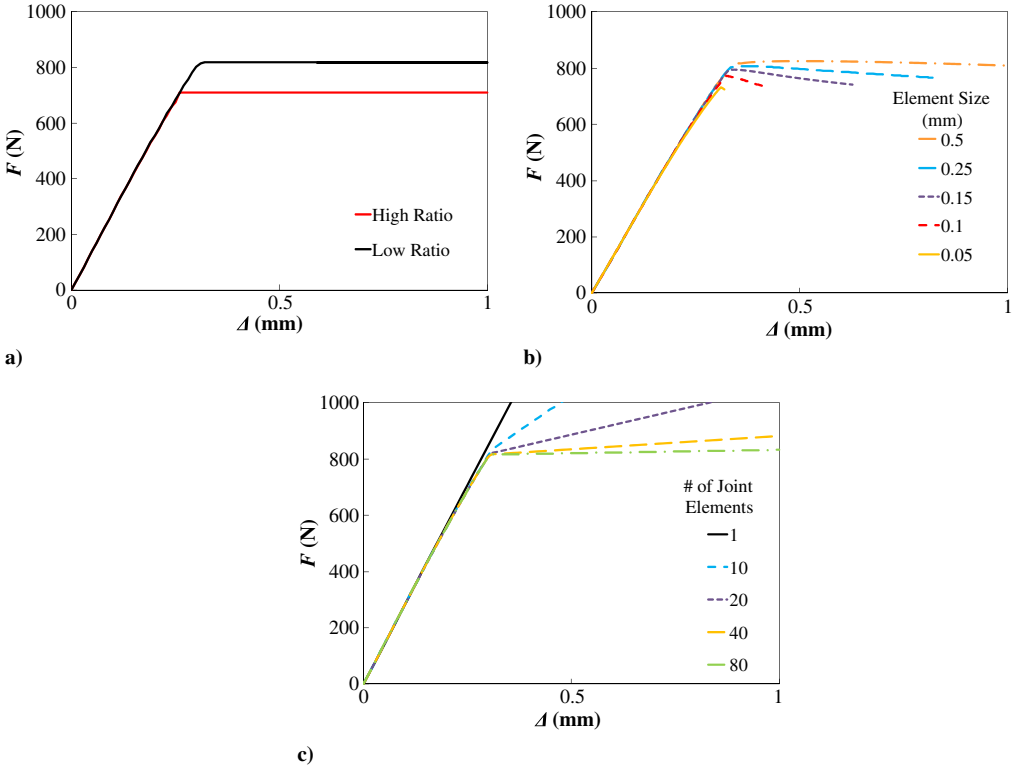

Fig. 13 Load displacement plots for the joint depicted in Fig. 10 with an elastic perfectly plastic adhesive with yield stress of 40 MPa: a) basing the constitutive properties on the peel to shear ratio of the highest stressed side and the lower side, b) elemental convergence for the 2-D dense mesh model, and c) joint element model.

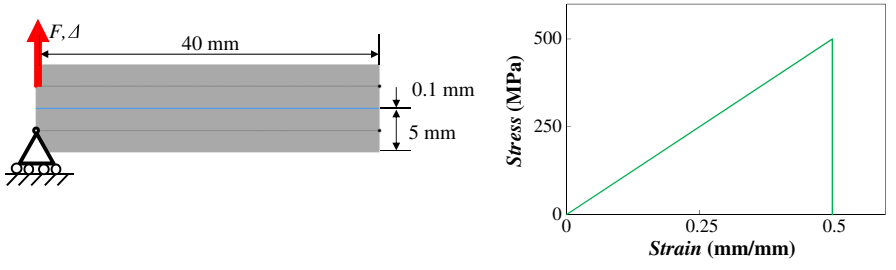

Fig. 14 Example of the peeling of a) a layered beam where the adhesive is modeled as b) linear until failure to demonstrate the joint element crack growth ability.

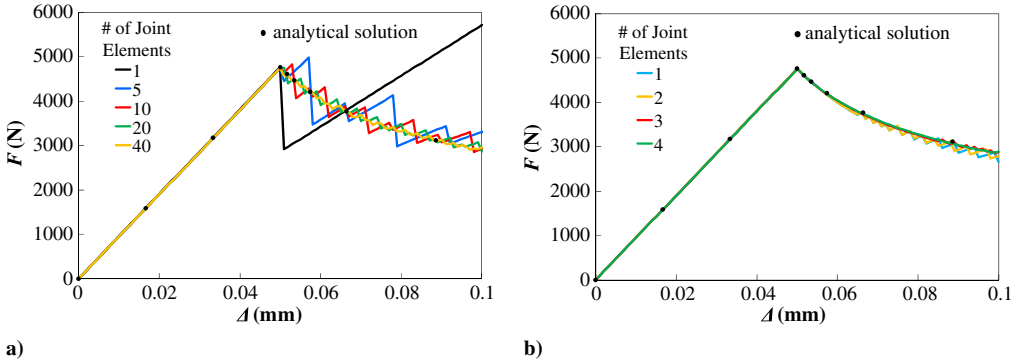

Fig. 15 Load displacement plots for the peeling of a layered beam with different numbers of joint elements using a) no remeshing and b) remeshing.

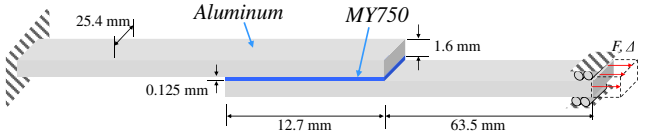

Fig. 16 Geometric parameters for a single lap joint tested by Harris and Adams [12].

an elastic perfectly plastic stress-strain relation. The adhesive, MY750, was characterized using bulk adhesive tensile tests, and the bulk adhesive stress-strain relation is shown in Fig. 17a.

The method outlined previously was followed to find the adhesive peel and shear stress-strain relations. First, the joint was analyzed with linear material properties and small rotations, and the peel to

Table 2 Material properties of the single lap joint adherends and adhesive [12]

Material	E, GPa	υ	0.2% proof stress, MPa
MY750	3.44	0.4	— —
Aluminum 2L73	70	0.34	430
Aluminum BB2hh	70	0.34	220
Aluminum BB2s	70	0.34	110

Table 3 Experimental and predicted strengths of the single lap joint

Adherend	Experimental strength, kN	Predicted strength, kN
2L73	4.8 ± 0.57	4.46
BB2hh	5.0 ± 0.38	4.52
BB2s	3.5 ± 0.32	5.00

shear ratio, ψ, was found to be 1.4. Using this value, the Young's modulus, and the Poisson's ratio, the bulk adhesive tensile data were converted to the peel and shear stress-strain relations shown in Fig. 17a. Using this, the joint was modeled with 20 beam elements and one joint element and was loaded in a displacement controlled manner until the peak load had been reached. The load-displacement plots for the single lap joints with different aluminum alloys are shown in Fig. 17b, and the results are compared with the experimental values found by Harris and Adams [12] in Table 3.

The joint with the 2L73 adherends failed without the adherends reaching the yield stress, whereas the BB2hh adherend joint had small amounts of adherend yielding and the BB2s joint was dominated by the effects of adherend yielding. Looking back to the single lap joint example of Sec. III.B, it can be seen that adherend yielding was not accurately captured by the current formulation of the joint element. As expected, the specimen with no signs of adherend yielding, 2L73, had a predicted strength well within the experimental error. The specimen with slight yielding, BB2hh, had a predicted strength slightly outside of the error range of the experiment. Finally, the BB2s adherend joint, being totally dominated by adherend yielding, had a predicted strength much higher than the experimental value.

However, if one again uses the single lap joint of Sec. III.B as an example, it can be surmised that if adherend plasticity were accounted for in a more accurate manner, the predicted peak load would be close to the elbow where the slope first drops, around 3 kN (where the adherend first reaches yielding). This would bring the prediction much closer to the experimental value.

If the elbow is taken to be the point of failure for the BB2s specimens, all three predictions would be lower than the experimental strength. There are several possibilities for this discrepancy. The first is that the actual joints had quite sizeable fillets at the ends of the adhesive. Although it has been shown that spring-type joint models, like the joint element, predict stresses within the bond line similar to those in joints with fillets [5], the fillet might reduce the stress enough to increase the strength slightly. Furthermore, the peel to shear ratio, ψ, was only approximated based on the linear elastic joint. However, large rotations and the accompanying nonlinearities change the peel to shear ratio, making it a function of the loading. Figure 18 shows the value of ψ as a function of the end displacement, Δ. It can be seen that the peel to shear ratio rapidly drops early on in the loading. Therefore, ψ could be adjusted to yield a more accurate answer.

This comparison showed that, as expected, the joint element is less than accurate with regards to adherend material nonlinearity.

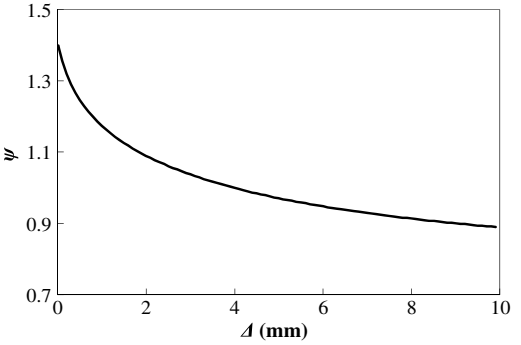

Fig. 18 Peel to shear stress ratio in the adhesive layer of the single lap joint as a function of end displacement.

However, the method devised to use bulk adhesive tensile data appears to have been successful in approximating the strength of this single lap joint. For most advanced composite joints, the adherends display brittle failure, so capturing adherend yielding is of secondary importance. However, a more precise model could be implemented to consider adherend damage.

IV. Conclusions

In this study, the linear elastic bonded joint element concept, introduced earlier [9], was extended to include large rotations, material nonlinearity [17], and adhesive failure. Large rotations, which occur commonly in adhesively bonded joints, were handled through a corotational formulation. This formulation separated the displacements into rigid body displacement and local deformations about a rotated local coordinate system. The local deformations are assumed to be small, and so a linear formulation can still be used. Material nonlinearities were included into the formulation [17]. However, a nonlinear-elastic model was adopted for simplicity. It was shown through examples that, although this model was sufficient for the adhesive layers with high stress concentrations and small plastic zones, it was not accurate for a description of the adherend materials, especially in the postyielded state. Problems arise with excessive adherend yielding, and it is suggested that the modeling of joints where adherend yielding is significant with the joint element be avoided. On a positive note, the load at which the adherend is fully yielded can be viewed as an upper limit load, whereas the onset of adherend yielding can be considered a lower limit.

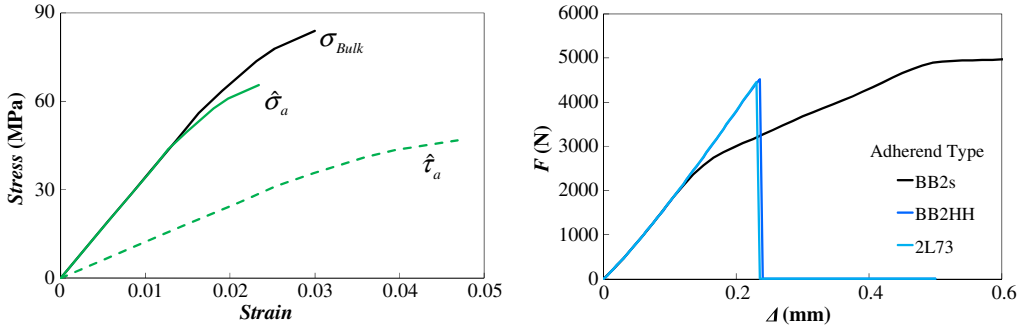

Fig. 17 Single joint element a) stress-strain relation for bulk adhesive, along with peel and shear components for a single lap joint with $\psi = 1.4$, and b) corresponding load-displacement plots.

Adhesive failure and crack formation and growth were accounted for through an internal remeshing process. The element with an internal crack was replaced by a subassembly with the failed adhesive removed. This method added to the computational steps that needed to be taken during the analysis, but decreased the number of elements needed to capture progressive failure.

Finally, methods of finding the nonlinear peel and shear stress-strain curves for the adhesive based on experimental procedures were outlined. First, using bulk adhesive tensile data, the response was broken up into shear and peel components for a certain joint configuration. This allowed the adhesive to be characterized with one test, but limited the shear and peel characterization to be specific to a certain joint type, geometry, and material. Next, the resemblance of the adhesive model to CZMs made it a natural candidate for fracture properties such as strength and fracture toughness. This was discussed in the formulation, although no examples of this kind were presented. This method of adhesive characterization has the disadvantage of requiring more tests, but seems to have fewer assumptions involved.

The model was first compared with a dense 2-D FEM and later compared with previously published experiments [12]. For the examples shown, the model was able to represent large rotations through a corotational formulation and matched up well with dense 2-D FEM models. The adhesive nonlinearities and failure were also captured accurately with the joint element model when compared with both experiments and the 2-D FEM model. An area of potential improvement for the model would be to include a modified von Mises flow theory as derived by Gali et al. [21] and used by Mortensen and Thomsen [5] and Harris and Adams [12], so that the ratio of shear to peel stress need not be considered constant and defined a priori. A critical weakness that was highlighted by the examples was the inability of the model to accurately capture adherend yielding. Euler–Bernoulli beam theory restricts the displacements to vary linearly in the thickness direction, which does not allow proper localization of yielding. Future work in this area includes applying a beam hinge formulation [29–36]. Another major future development required to improve the usefulness of the model is to extend the formulation to a shell-type element. This requires a different approach to solving the partial differential governing equations to obtain proper shape functions, but would vastly improve the utility of the model.

This model significantly reduces the number of degrees of freedom needed to predict important values like stress, strain, and strength when compared with traditional FE methods. Such reduced models then facilitate the integration of joint design into larger global-scale vehicle models without creating a significant bottleneck. This allows vital joint design to take place early on in the design phase, when design changes are relatively easy and inexpensive.

Acknowledgments

Portions of this work were financially supported by the Space Vehicle Technology Institute under Grant No. NCC3-989, jointly funded by NASA and the U.S. Department of Defense. The bulk of the financial support was provided by NASA John H. Glenn Research Center at Lewis Field through the NASA Graduate Student Researchers Project Fellowship. This paper is based on the Ph.D. dissertation of the first author, submitted to the Aerospace Engineering Department, University of Michigan, Ann Arbor, Michigan, February 2012.

References

[1] Volkersen, O., "Die Nietkraftverteilung in Zugbeanspruchten mit Konstanten Laschenquerschritten," *Luftfahrtforschung*, Vol. 15, 1938, pp. 41–47.

[2] Goland, M., and Reissner, E., "The Stresses in Cemented Joints," *Journal of Applied Mechanics*, Vol. 11, No. 1, 1944, pp. A17–A27.

[3] Hart-Smith, L. J., "Adhesive-Bonded Single-Lap Joints," NASA CR-112236, 1973, p. 116.

[4] Delale, F., Erdogan, F., and Aydinoglu, M. N., "Stresses in Adhesively Bonded Joints: A Closed-Form Solution," *Journal of Composite Materials*, Vol. 15, No. 3, May 1981, pp. 249–271. doi:10.1177/002199838101500305

[5] Mortensen, F., and Thomsen, O. T., "Analysis of Adhesive Bonded Joints: A Unified Approach," *Composites Science and Technology*, Vol. 62, 2002, pp. 1011–1031. doi:10.1016/S0266-3538(02)00030-1

[6] Zhang, J., Bednarcyk, B. A., Collier, C., Yarrington, P., Bansal, Y., and Pindera, M.-J., "Analysis Tools for Adhesively Bonded Composite Joints, Part 2: Unified Analytical Theory," *AIAA Journal*, Vol. 44, No. 8, 2006, pp. 1709–1719. doi:10.2514/1.15664

[7] Gustafson, P. A., and Waas, A. M., "A Bonded Joint Finite Element for a Symmetric Double Lap Joint Subjected to Mechanical and Thermal Loads," *International Journal for Numerical Methods in Engineering*, Vol. 79, No. 1, 2009, pp. 94–126. doi:10.1002/nme.v79:1

[8] Stapleton, S. E., and Waas, A. M., "Reduced-Order Modeling of Adhesively Bonded Joints Using an Enhanced Joint Finite Element," *Proceedings of the 52nd International SAMPE Symposium*, Paper No. 421stc-033, Salt Lake City, UT, 2010.

[9] Stapleton, S. E., Waas, A. M., and Arnold, S. M., "Functionally Graded Adhesives for Composite Joints," *International Journal of Adhesion and Adhesives*, Vol. 35, 2012, pp. 36–49. doi:10.1016/j.ijadhadh.2011.11.010

[10] Stapleton, S. E., and Waas, A., "Macroscopic Finite Element for a Single Lap Joint," *AIAA/ASME/ASCE/AHS/ASC 50th SDM Conference*, Palm Springs, CA, 2009.

[11] Kafkalidis, M. S., and Thouless, M. D., "The Effects of Geometry and Material Properties on the Fracture of Single Lap-Shear Joints," *International Journal of Solids and Structures*, Vol. 39, No. 17, 2002, pp. 4367–4383. doi:10.1016/S0020-7683(02)00344-X

[12] Harris, J. A., and Adams, R. A., "Strength Prediction of Bonded Single Lap Joints by Non-Linear Finite Element Methods," *International Journal of Adhesion and Adhesives*, Vol. 4, 1984, pp. 65–78. doi:10.1016/0143-7496(84)90103-9

[13] Banea, M. D., and da Silva, L. F. M., "Adhesively Bonded Joints in Composite Materials: An Overview," *Proceedings of the Institution of Mechanical Engineers, Part L: Journal of Materials Design and Applications*, Vol. 223, Jan. 2009, pp. 1–18.

[14] Belytscheko, T., and Hsieh, B. J., "Non-Linear Transient Finite Element Analysis with Convected Co-Ordinates," *International Journal for Numerical Methods in Engineering*, Vol. 7, 1973, pp. 255–271. doi:10.1002/(ISSN)1097-0207

[15] Crisfield, M. A., and Moita, G. F., "A Unified Co-Rotational Framework for Solids, Shells and Beams," *International Journal of Solids and Structures*, Vol. 33, Nos. 20–22, 1996, pp. 2969–2992. doi:10.1016/0020-7683(95)00252-9

[16] Crisfield, M. A., *Non-Linear Finite Element Analysis of Solids and Structures*, Wiley, New York, 1996, pp. 201–231.

[17] Stapleton, S. E., Waas, A. M., and Bednarcyk, B. A., "Modeling Progressive Failure of Bonded Joints Using a Single Joint Finite Element," *AIAA Journal*, Vol. 49, No. 8, 2011, pp. 1740–1749. doi:10.2514/1.J050889

[18] Guyan, R. J., "Reduction of Stiffness and Mass Matrices," *AIAA Journal*, Vol. 3, No. 2, 1965, pp. 380–380. doi:10.2514/3.2874

[19] Chen, S., and Pan, H. H., "Guyan Reduction," *Communications in Applied Numerical Methods*, Vol. 4, No. 4, July 1988, pp. 549–556. doi:10.1002/cnm.1630040412

[20] Chandrupatla, T. R., and Belegundu, A. D., *Introduction to Finite Elements in Engineering*, Prentice–Hall, Upper Saddle River, NJ, 1996, pp. 367–411.

[21] Gali, S., Dolev, G., and Ishai, O., "An Effective Stress/Strain Concept in the Mechanical Characterization of Structural Adhesive Bonding," *International Journal of Adhesion and Adhesives*, Vol. 1, No. 3, 1981, pp. 135–140. doi:10.1016/0143-7496(81)90036-1

[22] Sechler, E. E., *Elasticity in Engineering*, Dover, New York, 1968, pp. 1–411.

[23] Raghava, R., Caddell, R. M., and Yeh, G. S. Y., "The Macroscopic Yield Behaviour of Polymers," *Journal of Materials Science*, Vol. 8, No. 2, 1973, pp. 225–232. doi:10.1007/BF00550671

[24] Turon, A., Dávila, C. G., Camanho, P. P., and Costa, J., *An Engineering Solution for Using Coarse Meshes in the Simulation of Delamination with Cohesive Zone Models*, NASA TM-2005-213547, NASA Langley Research Center, Hampton, VA, 2005.

[25] Li, S., Thouless, M. D., Waas, A. M., Schroeder, J. A., and Zavattieri, P. D., "Use of a Cohesive-Zone Model to Analyze the Fracture of a Fiber-Reinforced Polymer-Matrix Composite," *Composites Science*

and Technology, Vol. 65, Nos. 3–4, 2005, pp. 537–549.
doi:10.1016/j.compscitech.2004.08.004

[26] Xie, D., Waas, A. M., Shahwan, K. W., Schroeder, J. A., and Boeman, R. G., "Fracture Criterion for Kinking Cracks in a Tri-Material Adhesively Bonded Joint Under Mixed Mode Loading," *Engineering Fracture Mechanics*, Vol. 72, No. 16, 2005, pp. 2487–2504.
doi:10.1016/j.engfracmech.2005.03.008

[27] Gustafson, P. A., *Analytical and Experimental Methods for Adhesively Bonded Joints Subjected to High Temperatures*, Ph.D. Dissertation, Univ. of Michigan, Ann Arbor, MI, 2008.

[28] Gustafson, P. A., and Waas, A. M., "The Influence of Adhesive Constitutive Parameters in Cohesive Zone Finite Element Models of Adhesively Bonded Joints," *International Journal of Solids and Structures*, Vol. 46, No. 10, 2009, pp. 2201–2215.
doi:10.1016/j.ijsolstr.2008.11.016

[29] Armero, F., and Ehrlich, D., "Numerical Modeling of Softening Hinges in Thin Euler–Bernoulli Beams," *Computers and Structures*, Vol. 84, Nos. 10–11, 2006, pp. 641–656.
doi:10.1016/j.compstruc.2005.11.010

[30] Armero, F., and Ehrlich, D., "An Analysis of Strain Localization and Wave Propagation in Plastic Models of Beams at Failure," *Computer Methods in Applied Mechanics and Engineering*, Vol. 193, Nos. 30–32, 2004, pp. 3129–3171.
doi:10.1016/j.cma.2003.07.015

[31] Ehrlich, D., and Armero, F., "Finite Element Methods for the Analysis of Softening Plastic Hinges in Beams and Frames," *Computational Mechanics*, Vol. 35, No. 4, 2005, pp. 237–264.
doi:10.1007/s00466-004-0575-z

[32] Vratanar, B., and Saje, M., "A Consistent Equilibrium in a Cross-Section of an Elastic–Plastic Beam," *International Journal of Solids and Structures*, Vol. 36, No. 2, 1999, pp. 311–337.
doi:10.1016/S0020-7683(97)00327-2

[33] Jirásek, M., "Analytical and Numerical Solutions for Frames with Softening Hinges," *Journal of Engineering Mechanics*, Vol. 123, No. 1, 1997, pp. 8–14.
doi:10.1061/(ASCE)0733-9399(1997)123:1(8)

[34] Wackerfuß, J., "Efficient Finite Element Formulation for the Analysis of Localized Failure in Beam Structures," *International Journal for Numerical Methods in Engineering*, Vol. 73, No. 9, 2008, pp. 1217–1250.

[35] Darvall, P. L., and Mendis, P. A., "Elastic-Plastic-Softening Analysis of Plane Frames," *Journal of Structural Engineering*, Vol. 111, April 1985, pp. 871–888.

[36] Bažant, Z. P., Pijaudier-Cabot, G., and Pan, J., "Ductility, Snapback, Size Effect, and Redistribution in Softening Beams or Frames," *Journal of Structural Engineering*, Vol. 113, Dec. 1987, pp. 2348–2364.

[37] Crocombe, A. D., "Global Yielding as a Failure Criterion for Bonded Joints," *International Journal of Adhesion and Adhesives*, Vol. 9, July 1989, pp. 145–153.

S. Pellegrino
Associate Editor